Detection of Lines in Synthetic Aperture Radar (SAR) Scenes

Olaf Hellwich[◆], Helmut Mayer[◆] and Gerhard Winkler[■]

[◆]Chair for Photogrammetry and Remote Sensing, Technical University Munich
Arcisstr. 21, D-80290 München, Germany
T: +49.89.2892.2677, F: +49.89.280.9573, EMail: olaf@photo.verm.tu-muenchen.de

[■]Mathematical Institute, Ludwig-Maximilians-Universität
Theresienstr. 39, D-80333 München, Germany
EMail: winkler@rz.mathematik.uni-muenchen.de

KEY WORDS: line extraction, Markov random fields, SAR, interferometry, GIS, feature extraction, fusion.

ABSTRACT:

Due to the speckle effect of coherent imaging the detection of lines in SAR scenes is considerably more difficult than in optical images. In spite of this, users of SAR data strongly demand their reliable and accurate detection. Therefore, a new approach to detect lines in noisy images using a Markov random field (MRF) model and Bayesian classification is proposed. The unobservable object classes of single pixels are assumed to fulfill the Markov condition, i.e. to depend on the object classes of neighboring pixels only. The influence of neighboring line pixels is formulated based on potentials derived from a random walk model. Locally, the image data is evaluated with a rotating template. As SAR intensity data is deteriorated by multiplicative noise, the response of the line detector is a normalized intensity ratio which results in a constant false alarm rate. The maximum a posteriori (MAP) estimate of the object parameters is approximated using simulated annealing. To obtain results with less computational effort the iterated conditional modes (ICM) estimator is applied to the maximum likelihood estimate. The approach integrates intensity, coherence from interferometric processing of a SAR scene pair, and given Geographic Information System (GIS) data.

1. INTRODUCTION

Lines in SAR scenes can be used for precision geocoding of SAR scenes or precision registration of SAR scenes with images acquired by other sensors (Leberl, 1990). Extracted lines are a basis to verify as well as update linear objects in GIS or in maps (Caves, 1993). Geologists use SAR scenes to detect lineaments, as the SAR sensor is very sensitive to geologic structures. The problem with lines in SAR scenes is that they are not only difficult to detect (Adair & Guindon, 1990; Hellwich & Streck, 1996), but that they are also partly invisible depending on the azimuth of the incident radiation (Hendry et al., 1988). In this paper as lines we regard narrow, elongated areas with approximately constant image intensity which are bounded by bright or dark regions. Note that this includes also lines which are bounded by a bright region on one side and a dark region on the other side.

In the past several approaches to the detection of linear structures in SAR scenes have been taken which can be differentiated into three groups depending on whether they mainly rely on a local evaluation of the intensity function, whether they consider more global criteria, or whether combine both. Local detectors either compute geometric properties like the first or the second derivative of the intensity function (e.g. Burns et al., 1981; Kwok, 1989), or they conduct a statistical evaluation of regions often defined by a rotating template (e.g. Caves et al., 1992; Lopes et al., 1993). Several investigations had the result that a local gradient computation is not suited for the detection of edges as the speckle effect of coherent imaging causes a noisy response of the edge operators (Geiss, 1984; Bellavia & Elgy, 1986; Adair & Guindon, 1990). Among the operators using statistical parameters those computing the intensity ratio of neighboring regions have been shown to give the most reasonable responses (Adair & Guindon, 1990; Caves, 1993). They have a constant false alarm rate, as the standard deviation of SAR intensity is equal to the intensity itself.

Approaches using more global criteria are the methods based on the Hough transform (Wood, 1985; Quegan et al., 1986; Skingley & Rye, 1987; Green et al., 1993), minimum-cost search (Bellavia & Elgy, 1986) or dynamic programming (Wood, 1985) to extract thin lines from SAR images. In spite of promising results the use of the Hough transform is limited, as in this context it can only be applied to the detection of straight lines.

Methods combining local operators with a more global evaluation are those developed by Samadani & Vesecky (1990) and Arduini et al. (1992). They use Bayes' theorem and a MAP estimation to combine a conditional probability to observe certain image data given a linear structure with a prior probability derived from the generic knowledge that lines are continuous and neighboring pixels depend on each other.

* This research was partially funded by Deutsche Agentur für Raumfahrtangelegenheiten (DARA) GmbH under contract 50EE9423.

Our new approach for the extraction of linear structures is related to these methods, as it is based on Bayesian inference and formulates prior knowledge about the continuity of lines as an MRF. To overcome the difficulties in the detection of linear structures the approach integrates generic knowledge about lines, given GIS data and the SAR scene data. The generic knowledge can be subdivided into three parts. The first part is the knowledge about the physical appearance of lines, i.e. narrow, elongated areas with approximately constant image intensity (see above). This type of knowledge is used to evaluate the scene data. In terms of Bayesian approaches it is therefore incorporated in the conditional probability density function (PDF) to observe scene data given a linear structure. The second part of knowledge about lines says that a line is continuous over a certain region of the scene. This means that a line can be assumed in a location where there is not enough physical evidence, if neighboring locations show sufficient evidence. This knowledge is derived from a random walk model and used in the prior PDF modeling the relationships between pixels of linear structures based on an MRF. In addition to the generic knowledge about the appearance of linear structures, the specific knowledge of the presence of a certain linear structure as given by a GIS is incorporated into the approach as third part of the knowledge. At pixels located at or close to where the GIS indicates a linear structure the probability to detect a linear structure having the corresponding direction is higher than at pixels at a larger distance.

As SAR data intensity is used optionally complemented by coherence resulting from an interferometric evaluation of a SAR scene pair. This feature is a step towards a utilization of the full information content of the complex SAR data.

In section 2 we explain how Bayes' theorem provides the framework to implement an approach to the detection of linear structures. Section 3 describes the modeling of the prior PDF of continuous lines based on an MRF and a random walk model for particles. In section 4 the conditional PDF for the local evaluation of the scene data is explained. Section 5 is dedicated to the computation of an optimal interpretation of the SAR scene by sampling from the posterior PDF. Finally, in section 6 the results of tests of the algorithm are presented and, in section 7, conclusions and recommendations are given.

2. BAYESIAN LINE EXTRACTION USING MARKOV RANDOM FIELDS

The extraction of linear structures can be based on a Bayesian approach to solve the inverse problem of computing the location of lines from the measured scene data (Oliver, 1991; Koch & Schmidt, 1994; Winkler, 1995). The posterior probability density of the object parameters given the scene data is derived according to Bayes' theorem

$$p(\boldsymbol{\varepsilon}|\boldsymbol{y}) = \frac{p(\boldsymbol{y}|\boldsymbol{\varepsilon}) \cdot p(\boldsymbol{\varepsilon})}{p(\boldsymbol{y})} \tag{2.1}$$

where $\boldsymbol{\varepsilon}$ is the object parameter vector. $\boldsymbol{\varepsilon}$ contains one element ε_s for each site $s \in S$, i.e. regularly for each pixel of the scene S. Depending on whether the object is described by one or more parameters at each site, ε_s can be a scalar or a vector. For the time being we assume that ε_s is a scalar taking the state "line site" or "no-line site", i.e. the state space is $E_s = \{"line\ site", "no-line\ site"\}$. Sometimes we will have to refer to a site object parameter variable which takes a specific state, i.e. we will have to make a difference between a variable and its instantiation. In formulas we will express this as $E_s=\varepsilon_s$. The scene data vector $\boldsymbol{y}$ also contains one element y_s for each site of the scene. As our goal is the combined evaluation of intensity and coherence, $\boldsymbol{y}_s$ is vectorial. The probability density of the data vector $p(\boldsymbol{y})$ can be omitted, because it is independent of $\boldsymbol{\varepsilon}$; then Bayes' theorem becomes

$$p(\boldsymbol{\varepsilon}|\boldsymbol{y}) \propto p(\boldsymbol{y}|\boldsymbol{\varepsilon}) \cdot p(\boldsymbol{\varepsilon}). \tag{2.2}$$

The prior probability density $p(\boldsymbol{\varepsilon})$ and the conditional probability density of the scene data given the object parameters $p(\boldsymbol{y}|\boldsymbol{\varepsilon})$ are to be formulated according to our knowledge about linear structures and the scene formation process.

To simplify the estimation of the object parameter at a site s we assume the object parameters as well as the scene data to be MRF. A random field is Markovian, if for all $\boldsymbol{x}$

$$p(x_s|x_r, r \neq s) = p(x_s|\partial x_s) \tag{2.3}$$

where ∂x_s is a neighborhood of s considerably smaller than the complete scene. Using this assumption, the conditional density of an object parameter value at a site s is

$$p(\varepsilon_s|y_s, \partial y_s, \partial \varepsilon_s) \propto p(y_s|\partial y_s, \varepsilon_s) \cdot p(\varepsilon_s|\partial \varepsilon_s). \tag{2.4}$$

In the case of $\partial y_s = \{\}$, i.e. independence of the data from its neighbors, (2.4) simplifies to

$$p(\varepsilon_s|y_s, \partial \varepsilon_s) \propto p(y_s|\varepsilon_s) \cdot p(\varepsilon_s|\partial \varepsilon_s). \tag{2.5}$$

This is strictly true only for uncorrelated data.

For further reasoning we use the equivalence of MRF and neighborhood Gibbs fields. In Gibbsian form the probability density $p(\boldsymbol{x})$ is expressed as

$$p(\boldsymbol{x}) = \frac{\exp\{-H(\boldsymbol{x})\}}{\sum_{z \in X_c} \exp\{-H(z)\}} \tag{2.6}$$

where $\boldsymbol{X}_C$ is the configuration space of $\boldsymbol{X}$, i.e. the set containing all possible instantiations of $\boldsymbol{X}$. The energy function $H(\boldsymbol{x})$ of an MRF which is equivalent to a neighborhood Gibbs field is

$$H(\boldsymbol{x}) = \sum_{A \subset S} U_A(\boldsymbol{x}) \tag{2.7}$$

where each clique A is a subset of the scene S containing sites with a certain geometric configuration, and U_A is a potential of A. The conditional probability density at a site s results from a summation over the set K_s of all cliques A containing s

$$p(x_s|\partial x_s) \propto \exp\{-H_s(x_s|\partial x_s)\} \tag{2.8}$$

where $H_s(x_s|\partial x_s) = \sum_{A \in K_s} U_{As}(x_s|\partial x_s)$. Now we are able to express (2.5) in terms of energies:

$$H_s(\varepsilon_s|y_s, \partial \varepsilon_s) = H_s(y_s|\varepsilon_s) + H_s(\varepsilon_s|\partial \varepsilon_s). \tag{2.9}$$

The scene data $\boldsymbol{y}$ is a vectorial MRF $y_s{}^T = \left(y_{I_s} \quad y_{C_s}\right)$ where y_{I_s} and y_{C_s} are the intensity and the coherence, respectively. If y_{I_s} and y_{C_s} are considered as independent, (2.9) can be written as (Schistad Solberg & Taxt, 1994)

$$H_s\left(\varepsilon_s \middle| y_{I_s}, y_{C_s}, \partial\varepsilon_s\right) = H_s\left(y_{I_s}\middle|\varepsilon_s\right) + H_s\left(y_{C_s}\middle|\varepsilon_s\right) + H_s\left(\varepsilon_s\middle|\partial\varepsilon_s\right) \tag{2.10}$$

The components of (2.10) are explained in detail in chapters 3 and 4.

3. PRIOR KNOWLEDGE ABOUT LINEAR STRUCTURES

Two types of prior knowledge are expressed by the prior PDF: the generic knowledge about continuous, elongated linear structures, and the specific knowledge about certain linear structures given by a GIS.

3.1 Generic Knowledge About Continuous Curvilinear Structures

The model of continuous curvilinear structures was inspired by the work of Williams & Jacobs (1995) about stochastic completion fields. They describe occluded, but perceptually salient contours with random walks of particles having its source at unoccluded points of the contours. The path most probably taken by the particles is assumed to be the location of the illusory contour. We use a similar random walk model to derive the potentials of two-pixel cliques of a neighborhood Gibbs field. A neighboring line site t is treated as a source of random walks whereas the site s, i.e. in terms of MRF the site for which the energy is computed, serves as a sink. The more particles pass through s the higher is the probability that s is a line site.

In section 2 we assumed a site has the object parameter values ε_s "line site" or "no-line site". We will now refine this rather general model. A line or a migrating particle passing a site has more properties than only its quality of being a line or a line particle. Its path has a certain direction and curvature which can be estimated as well. Thus the state space $\boldsymbol{E}_s$ of the object parameters ε_s becomes

$$\boldsymbol{E}_s = \left\{ "no-line", "line\left(\theta_i, \kappa_j\right)" : i \in \{1,\ldots I\}, j \in \{1,\ldots J\} \right\} \tag{3.1}$$

where θ_i are I discrete directions equally spaced in the interval $[0,\pi[$, and κ_j are J discrete curvatures equally spaced in the interval $[-\kappa_{max}, \kappa_{max}]$, and κ_{max} is the magnitude of a maximum curvature. Note that ε_s is still a scalar.

The particles of the random walk originate at a certain position (x_0, y_0) in the x, y-coordinate plane and possess a direction θ_0 and a curvature κ_0 (Fig. 3.1). During each step of the random walks x, y, θ, and κ are updated according to

$$\begin{aligned} \dot{x} &= \bar{l} \cdot \cos\left(\theta + l\frac{\kappa}{2}\right) \\ \dot{y} &= \bar{l} \cdot \sin\left(\theta + l\frac{\kappa}{2}\right) \\ \dot{\theta} &= l\kappa + \hat{\theta}\left(0,\sigma_\theta\right) \\ \dot{\kappa} &= \hat{\kappa}\left(0,\sigma_\kappa\right) \end{aligned} \tag{3.2}$$

where $\bar{l} = \frac{l}{\kappa}\sin\left(l \cdot \frac{\kappa}{2}\right)$. $\dot{x}, \dot{y}, \dot{\theta}$ and $\dot{\kappa}$ specify the change in position, direction and curvature, l is the step size, and $\hat{\theta}$ and $\hat{\kappa}$ are normally distributed, zero-mean random variables with standard deviations σ_θ and σ_κ. With each step a certain fraction of the particles decays. The probability of decay is $1 - e^{-\frac{l}{\tau}}$ at each step where τ is a decay parameter being large for strong or long lines and small for weak or short lines. Figs. 3.2 and 3.3 show examples of simulated random walks. At each grid point particles have been counted differentiated by state according to (3.1). For reasons of better presentation the curvature-state counts have been combined. The resulting count for each direction state is shown by a line in the appropriate direction with a length proportional to the logarithm of the count.

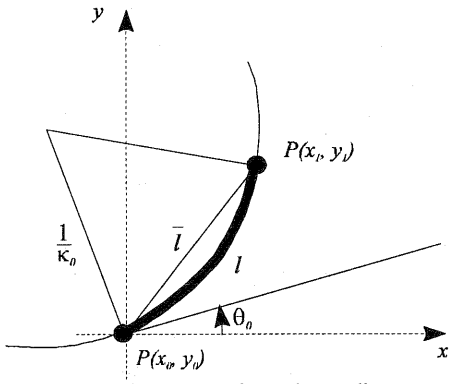

Fig. 3.1. One step of a random walk.

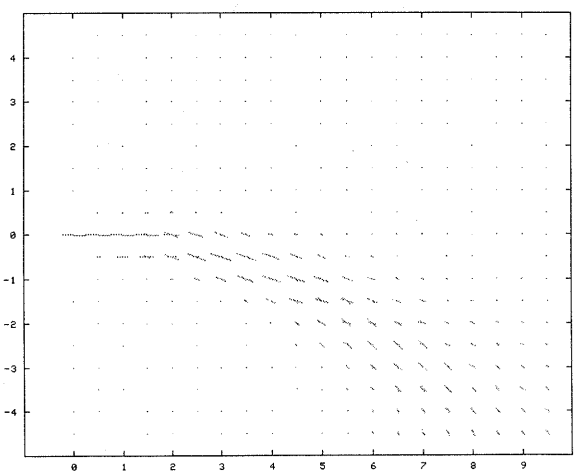

Fig. 3.2. Random walk simulation with κ_0=-0.1, τ=30, σ_θ=0.02, σ_κ=0.02.

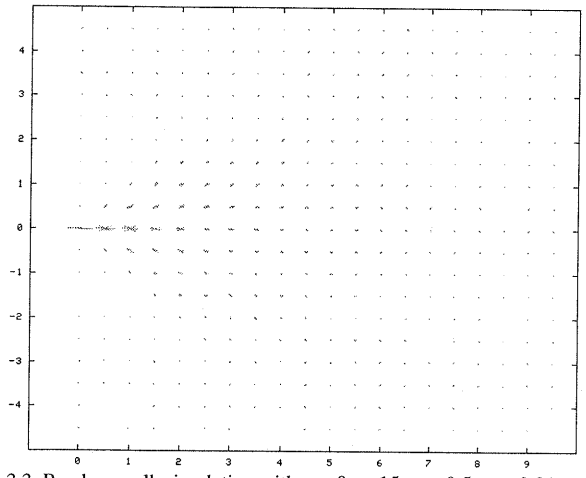

Fig.3.3. Random walk simulation with κ_0=0, τ=15, σ_θ=0.5, σ_κ=0.01.

For the computation of the energies $H_s(\varepsilon_s|\partial\varepsilon_s)$ a neighborhood system of two-site cliques is defined (Koch & Schmidt, 1994). Each site has neighbors of varying order forming a clique with each of those neighbors. Fig 3.4 shows the neighborhood system of site s up to order 5. For an element ε_s of the state space E_s, the counts of the random walk model are summed clique by clique. Each count depends on the parameter values ε_t and ε_s, i.e. on direction and curvature in the neighboring site t and the direction and curvature proposed at site s, as well as on the location of t with respect to s. If ε_t is "*no line*", the counts at s are *0* independent of ε_s. High counts for ε_s indicate a high probability of ε_s, as the presence of a neighboring line site supports the presence of a line with a certain direction and curvature.

5	4	3	4	5
4	2	1	2	4
3	1	*s*	1	3
4	2	1	2	4
5	4	3	4	5

Fig. 3.4. Neighborhood system for a two-site clique Gibbs field. Site s and another site form a two-site clique of neighborhood order n shown in the graph.

We now extend our two-site clique neighborhood model, as a line should also make certain neighboring lines improbable. This is because line sites parallel to a directly neighboring line site do not conform with the elongatedness of lines. It can be modeled with the same type of random walks. We only imagine a different type of particles, called inhibiting particles, diffusing perpendicularly to the direction of a line site. The particles inhibit the presence of lines perpendicular to the direction of propagation in the same way the particles used before supported the presence of lines in the direction of propagation. Therefore, the corresponding counts make the presence of those lines improbable and are subtracted from the supporting counts.

Introducing a one-site clique containing only s, we can control the overall probability of a line independent from the state of neighboring sites.

Hence, in agreement with (2.8), $H_s(\varepsilon_s|\partial\varepsilon_s)$ is computed from

$$H_s(\varepsilon_s|\partial\varepsilon_s) = \begin{cases} -\ln(C) & \text{if } C \geq 1 \\ -\ln(1) & \text{if } C < 1 \end{cases} \qquad (3.3)$$

$$C = C_{A_1}(\varepsilon_s) + \sum_{A_2} C_{A_2}(\varepsilon_s|\varepsilon_t; s,t \in A_2)$$

where C_{A_1} is the count-equivalent of the one-pixel clique:

$$C_{A_1}(\varepsilon_s) = \begin{cases} c_l & \text{if } \varepsilon_s = "line(\theta_s, \kappa_s)" \\ c_n & \text{if } \varepsilon_s = "no\text{-}line" \end{cases}.$$

c_l and c_n are empirically chosen "basic currents" which control the overall probability of line and no-line sites. $\sum_{A_2} C_{A_2}$ is the sum of the counts of the two-site cliques containing s.

3.2 Specific Knowledge from GIS Data

The intention is to use GIS data to support the extraction of linear structures. It may for instance be known that a road is crossing the imaged area, and an approximate registration of the SAR scene and the GIS data may be given. Around the projection of the road center line into the SAR scene the probability to detect a line with the direction and curvature of the road center line should be increased. These facts have to be used to compute the energy of the prior PDF.

It is known that the registration of SAR and GIS data can only be accurate to a limited degree. What is more, the decision about the exact location of the linear structure in the results of the algorithm has to depend on the SAR data and not on the given geographic information. Therefore, a corridor symmetrical around the object center line is defined inside of which the probability of the object class $\varepsilon_s = line(\theta_i, \kappa_i)$ is uniformly increased. θ_i, κ_i are the direction and curvature of the object center line at the point i closest to site s (Fig. 3.5).

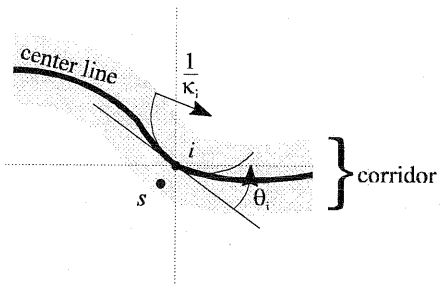

Fig. 3.5. Corridor around an object center line in which the detection of lines with direction and curvature of the object center line is increased.

The parameters of the algorithm are the width of the corridor which depends on the accuracy of the registration, and the amount by which the probability of line detection is increased. The increase in probability is taken into account by changing the computation of C_{A_1} in (3.3) to

$$C_{A_l}(\varepsilon_s)=\begin{cases} c_l+c_c & \text{if } \varepsilon_s=\text{"}line(\theta_s,\kappa_s)\text{"}\wedge \\ & \quad s\in corridor\wedge\theta_s=\theta_i\wedge\kappa_s=\kappa_i \\ c_l & \text{if } \varepsilon_s=\text{"}line(\theta_s,\kappa_s)\text{" otherwise} \\ c_n & \text{if } \varepsilon_s=\text{"}no\text{-}line\text{"} \end{cases} \quad .(3.4)$$

c_c is an "additional current" due to the presence of a GIS object. The membership of a site in a corridor and the state which is affected by this are computed prior to the line extraction and stored in a raster map.

4. LOCAL DATA EVALUATION

According to (2.10) we are dealing with two types of data: the SAR intensity and the interferometric coherence. Both are evaluated in a similar manner which is treated in this section.

For edge detection in SAR intensity data the ratio edge detector has been shown to give the best measure of edge strength. It corresponds with the multiplicative noise characteristics of the data and results in a constant false alarm rate (Touzi et al., 1988; Bovik, 1988; Adair & Guindon, 1990; Caves, 1993). Our approach is also based on the ratio detector.

In general the ratio operator compares two small regions of the image, e.g. the left and the right half of a window. In each of the two regions the averages of the intensities are computed. The normalized ratio output is the ratio of the two averages using the larger one as the denominator:

$$r=\frac{\min(\langle I_1\rangle,\langle I_2\rangle)}{\max(\langle I_1\rangle,\langle I_2\rangle)} \qquad (4.1)$$

where $\langle I_1\rangle$ and $\langle I_2\rangle$ are the mean intensities. If r is close to 1, the regions do not contrast. If r approaches 0 and the intensity is homogeneous in both regions, there is a discontinuity along the boundary of the regions.

To detect a line a detector mask is defined which consists of three regions (Lopes et al., 1993): a line region and two regions at the sides of the line region (see Fig. 4.1). Curved lines of varying widths can be considered. The detector masks are generated prior to the processing of the scene for a set of line directions, curvatures and widths. They correspond to the discrete line directions and curvatures defined by (3.1).

The ratio operator is applied to all combinations of the detector mask regions. The line detector has to be prevented from giving a response to the location of edges or strong scatterers. Therefore, we follow a procedure similar to the one proposed by Lopes et al. (1993). In case a line is present at the processed location the line region is homogenous, which means that the pixel intensities do not vary much. For SAR intensity data, this condition can be checked by computing the coefficient of variation

$$v_I=\frac{\sigma_I}{\langle I\rangle} \qquad (4.2)$$

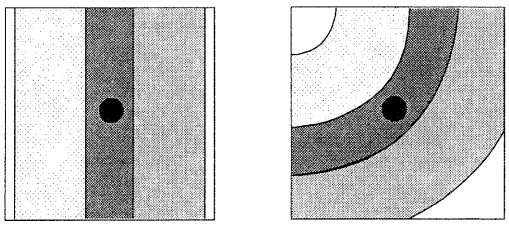

Fig. 4.1. Geometries of detector masks for line detection. The spot in the center of the window marks the site to be investigated.

where $\langle I\rangle$ is the mean intensity and σ_I is the standard deviation of the intensity I. As $\sigma_I=I$ for homogenous regions, v_I of the investigated region has to be less than a threshold somewhat larger than 1 if the region does not contain any structures.

As the average values of the side regions may be influenced by the presence of strong scatterers, they are replaced by the median of the intensity values. It is checked whether the line intensity differs significantly from the intensities of both side regions by computing the ratios between the line region and the side regions. These ratios are tested for membership in the ratio distribution of regions without contrast, i.e. regions which have the same intensities. For this purpose we adopted a threshold derived from the PDF of the normalized ratio r which is based on SAR intensity statistics (Caves, 1993):

$$p(r|I_1,I_2,N_1,N_2,L)=\frac{\Gamma(N_1L+N_2L)}{\Gamma(N_1L)\Gamma(N_2L)}\left[\frac{\left(\frac{rI_2}{I_1}\cdot\frac{N_1}{N_2}\right)^{N_1L}}{\left(1+\frac{rI_2}{I_1}\cdot\frac{N_1}{N_2}\right)^{N_1L+N_2L}}\right.$$

$$\left.+\frac{\left(\frac{rI_1}{I_2}\cdot\frac{N_2}{N_1}\right)^{N_2L}}{\left(1+\frac{rI_1}{I_2}\cdot\frac{N_2}{N_1}\right)^{N_1L+N_2L}}\right]\frac{1}{r}\,. \qquad (4.3)$$

I_1 and I_2 are the intensities, N_1 and N_2 are the number of pixels in both regions, and L is the number of looks per pixel. L is computed by dividing the ground pixel size by the size of the resolution element of the sensor. Thus N_1L is the number of independent samples. Fig. 4.2 shows the PDF for various contrasts I_1/I_2. It is strictly valid only for ratios of averages and not of medians, but tests have shown that it is a good approximation. Two regions are considered to be significantly different if $r<r_1$, where r_1 is a threshold derived from

$$\int_0^{r_1} p(r|I_1=I_2,N_1,N_2,L)dr=0.05. \qquad (4.4)$$

If the line region is significantly different from both side regions, a line site has been found. Then the side regions are checked for similarity which is assumed, if $r>r_2$ where r_2 is a threshold derived from

$$\int_0^{r_2} p(r|I_1=I_2,N_1,N_2,L)dr=0.5. \qquad (4.5)$$

If the side regions are not similar, the ratio response of the operator is the larger one of the normalized ratios between the line region and one of the side regions, i.e. the ratio towards the less contrasting side. If the side regions are similar, a common median and a normalized ratio between the line and the united side regions is computed.

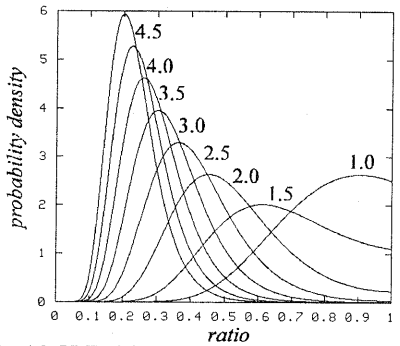

Fig. 4.2. PDF of the normalized intensity ratio for various contrasts I_1/I_2.

From the resulting ratio responses the energy values of the intensity data $H_s(y_{I_s}|\varepsilon_s)$ are derived. Instead of the intensity of a pixel we utilize the ratio r_s to compute H_s, i.e. we set

$$H_s(y_{I_s}|\varepsilon_s) = H_s(r_s|\varepsilon_s) \tag{4.6}$$

where r_s is a derived observation.

A reasonable way to derive energies from observations is to assume normally distributed observations. For those the energy H is computed from (Köster, 1995)

$$H(x) = \frac{(x-\mu_x)^2}{2\sigma_x^2} \tag{4.7}$$

where μ_x and σ_x are mean and standard deviation of the normal distribution. From (4.3) it is known that the ratio is not normally distributed. Nevertheless using (4.3) instead of (4.7) poses difficulties, as we do not have any reasonable assumption about the line contrast I_1/I_2 a line might have. Furthermore, r_s was computed using several tests for region homogeneity and similarity which is why the distribution of r_s is not strictly (4.3). Therefore, we propose to compute $H_s(r_s|\varepsilon_s)$ from (4.7) where $\mu_{r_s}=0$ for line sites (ε_s ="$line(\theta,\kappa)$"; cf. (3.1)) and σ_{r_s} is roughly adjusted to the line contrast in the processed scene.

For no-line sites (ε_s ="$no-line$") we propose to use a uniform distribution instead of a normal distribution

$$H_s(x) = \text{constant} \tag{4.8}$$

This idea is borrowed from maximum-likelihood classification of multispectral imagery where for the land-use classes normal distributions are utilized (e.g. Richards, 1993). If the maximum density $p_{\max}(y_s|\varepsilon_s)$ is less than a threshold T, pixel s with the multispectral data vector y_s will not be classified. Such a pixel corresponds to a no-line site in our case. A reasonable value for T can be derived from (4.7) when a maximum ratio $r_{\max}$ for line pixels is assumed. $r_{\max}$ can be determined from a sample image.

We are now able to formulate the complete energy function of the intensity ratio:

$$H_s(r_s|\varepsilon_s) = \begin{cases} \dfrac{r_s^2}{2\sigma_r^2} & \text{if } s \text{ is a line site} \\ \dfrac{r_{\max}}{2\sigma_r^2} & \text{if } s \text{ is a no-line site} \end{cases} \tag{4.9}$$

The PDF of this energy function is illustrated by Fig. 4.3. The bell-shaped line shows the PDF of a line site based on a normal distribution, and the horizontal line shows the PDF of a no-line site. Using $H_s(r_s|\varepsilon_s)$ without a prior energy $H_s(\varepsilon_s|\partial\varepsilon_s)$, which is the case with any maximum-likelihood classification, is equivalent to thresholding the response of the ratio operator.

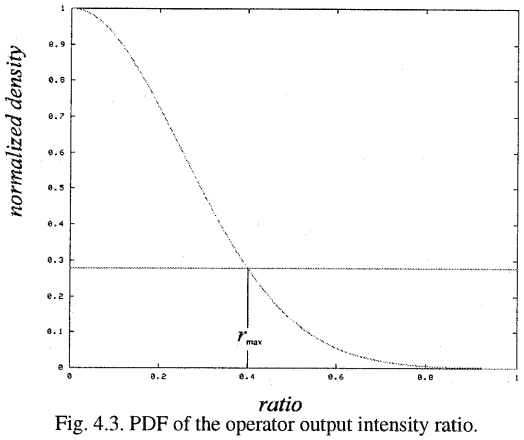

Fig. 4.3. PDF of the operator output intensity ratio.

The coherence is processed in a similar manner as the intensity. The data is evaluated applying the same detector masks, but instead of the ratio the difference is computed. The checks for homogeneity, dissimilarity and similarity of regions are essentially the same as for intensity data except that the thresholds are derived much more empirically, as the statistical properties of coherence data are not as well known as those of intensity data (but cf. Tough et al., 1994a; 1994b). $H_s(y_{C_s}|\varepsilon_s) = H_s(d_s|\varepsilon_s)$ is computed according to (4.9) where all ratios r are replaced by differences d.

5. ESTIMATION OF THE OBJECT PARAMETERS

Our goal is the estimation of the object parameter vector $\boldsymbol{\varepsilon}$ (cf. (3.1)). An optimal $\boldsymbol{\varepsilon}$ is the one that results in a global maximum of $p(\boldsymbol{\varepsilon}|\mathbf{y})$ which is difficult to determine owing to the overwhelmingly large configuration space of $\boldsymbol{\varepsilon}$. Presently, we apply two methods two approximate the global optimum. As an approximation to a MAP estimation we use simulated annealing in combination with Gibbs or Metropolis sampling, and as a faster deterministic approach which is only guaranteed to find a local optimum Besag's ICM estimator. As these methods have been intensively treated in various publications (e.g. Geman & Geman, 1984; Busch, 1992; Koch & Schmidt, 1994; Winkler, 1995; Guyon, 1995; Köster, 1995), we will only give a brief description.

The sites are visited once per iteration in a random sequence. For simulated annealing the object parameters of the sites are randomly initialized with the proportions between line and no-line sites given by c_l and c_n according to (3.3). The computation of probability densities from energies is conducted as

$$p(x_s|\partial x_s) \propto \exp\left\{-\frac{H(x_s|\partial x_s)}{T}\right\} \qquad (5.1)$$

(cf. (2.8)) where T is a temperature variable. It is decreasing according to a cooling schedule

$$T = \frac{1}{C \cdot \ln i} \qquad (5.2)$$

where C is a cooling constant and i is the index of the current iteration. A theoretical value for C which ensures that the simulated annealing procedure finally leads to a global optimum exists, but it would require prohibitorily many iterations until stability and the optimum were reached. Therefore, fast cooling with an empirical value of C close to 1 was used.

For the ICM algorithm ε is initially set to the maximum likelihood interpretation of the image which is the result when each site is visited once and E_s is set to the object parameter ε which gives the minimum energy $H_s(y_s|\varepsilon_s)$, i.e. the maximum conditional density $p_{\max}(y_s|\varepsilon_s)$ of the observations given the object parameter. During ICM estimation the discrete conditional PDF is computed in the same way as for the Gibbs sampler. In each site E_s is set to the value ε with the maximum conditional posterior probability $p(\varepsilon_s|y_s,\partial\varepsilon_s)$. The algorithm stops when $p(\varepsilon|y)$ reaches a maximum, i.e. when no sites change their states any more.

6. RESULTS

The model of continuous curvilinear structures based on random walk simulations was tested by Gibbs sampling from the prior PDF $p(\varepsilon)$. For a 128 by 128 pixels image we obtain results such as the one shown in Fig. 6.1. The picture shows thin curvilinear features some of which are connected starting to form a network. This is not quite what would be expected of a road network. But consider that the model is based on comparatively small neighborhoods. What is more, Gibbs sampling means drawing random samples from the complete configuration space where transitions between the most probable states can only occur by changing the state of single sites, i.e. by obtaining less probable states. Therefore, this result is acceptable.

A TOPSAR airborne data set consisting of intensity (Fig. 6.2) and coherence (Fig. 6.3) was evaluated. Fig. 6.4 shows the response of the intensity-ratio operator based on detector masks for 3 pixel wide dark lines aiming at the detection of narrow roads. This is the information contained in the data which is handed over to the Bayesian inference procedure. Fig. 6.5 shows the result of a maximum likelihood classification of the intensity data which is equivalent to thresholding the intensity-ratio response of Fig. 6.4. The result is noisy, lines vary strongly in width and direction, and have several gaps. Note that this is a result obtained without using prior knowledge about the continuity of linear structures. Fig. 6.6 shows the result of 25 iterations of simulated annealing. Many of the gaps have been closed even in locations where the ratio image does not show a significant response of the ratio line detector, the width of the lines usually is small and does not vary much, and the detected directions are stably following the directions of the lines. This demonstrates the usefulness of the line model.

Fig. 6.7 results from 25 iterations of simulated annealing evaluating both intensity and coherence data. In comparison to Fig. 6.6 an improvement of the line extraction can be realized. Fig. 6.8 shows the corridor generated from a road center line given in a GIS. Once this data is included into the estimation procedure this road can be detected more easily (see Fig. 6.9).

7. CONCLUSIONS AND RECOMMENDATIONS

We proposed a new approach for the extraction of linear structures from SAR intensity and coherence data in a Bayesian framework using an MRF to model continuous curvilinearity. Test results demonstrate the plausibility of the MRF line model as well as the usefulness of combining SAR intensity with coherence and given GIS data when extracting linear objects.

Further tests of the approach are necessary. Presently, we consider improvements regarding speed and scale space integration. Computational speed could be gained by using local highest confidence first (LHCF) estimation (Chou et al., 1993) which would implicitly relate the algorithm to line following algorithms. Scale space requirements can presently be met by using different line widths in the detector masks. A more effective way would be the use of an image pyramid or a multiresolution MRF model (Lakshmanan & Derin, 1993; Bouman & Shapiro, 1994). We intend to make these topics subjects of future publications.

ACKNOWLEDGMENTS

We thank Vexcel Corporation, Boulder, for providing the test data set.

REFERENCES

Adair M., Guindon B. [1990]: Statistical Edge Detection Operators for Linear Feature Extraction in SAR Images, Canadian Journal of Remote Sensing, Vol. 16, No. 2, pp. 10-19.

Arduini F., Dambra C., Regazzoni C. S. [1992]: A Coupled MFR Model for SAR Image Restoration and Edge-Extraction, IGARSS '92, Houston, Vol. 2, pp. 1120-1122.

Bellavia G., Elgy J. [1986]: Spatial Feature Extraction from Radar Imagery, Symposium on Remote Sensing for Resources Develop-

ment and Environmental Management, Enschede, pp. 99-102.

Bouman C. A., Shapiro M. [1994]: A Multiscale Random Field Model for Bayesian Image Segmentation, IEEE Transactions on Image Processing, Vol. 3, No. 2, pp. 162-177.

Bovik A. C. [1988]: On Detecting Edges in Speckle Imagery, IEEE Transactions on Acoustics, Speech, and Signal Processing, Vol. 36, No. 10, pp. 1618-1627.

Burns J., Huertas A., Nevatia R. [1981]: Object Detection in Synthetic Aperture Radar Images, Image Understanding Research, Proc., Univ. of Southern California, pp. 38-51.

Busch A. [1992]: Bayes-Statistik und Markoff-Felder für die Restaurierung digitaler Bilder, Deutsche Geodätische Kommission, C, No. 396, 74 pages.

Caves R. G., Harley P. J., Quegan S. [1992]: Matching Map Features to Synthetic Aperture Radar (SAR) Images Using Template Matching, IEEE Transactions on Geoscience and Remote Sensing, Vol. 30, No. 4, pp. 680-685.

Caves R.G. [1993]: Automatic Matching of Features in Synthetic Aperture Radar Data to Digital Map Data, Ph.D. thesis, University of Sheffield, Dept. of Applied and Computational Mathematics.

Chou P.B., Cooper P.R., Swain M.J., Brown C.M., Wixson L.E. [1993]: Probabilistic Network Inference for Cooperative High and Low Level Vision, in: Chellappa R., Jain A., Markov Random Fields. Theory and Applications, Academic Press, Boston, pp. 211-243.

Geman S., Geman D. [1984]: Stochastic Relaxation, Gibbs Distribution, and the Bayesian Restoration of Images, IEEE Transactions on Pattern Analysis and Machine Intelligence, Vol. PAMI-6, No. 6, pp. 721-741.

Giess S. C., 1984: Edge detection in SAR imagery using gradient operators, Royal Signals and Radar Establishment, St. Andrews Rd., Great Malvern, Worcestershire, England, RSRE Memorandum No. 3743.

Green I. J., Sawyer F. G., Dunster S. B. [1993]: SAR Image Feature Extraction System - A Pre-Operational Application of ERS-1 SAR, Operationalization of Remote Sensing, Proc., Enschede, Vol. 5, pp. 23-32.

Guyon X. [1995]: Random Fields on a Network. Modeling, Statistics, and Applications, Springer Verlag, New York, 255 pages.

Hellwich O., Streck C. [1996]: Linear Structures in SAR Coherence Data, IGARSS '96, Lincoln, in press.

Hendry A., Quegan S., Wood J. [1988]: The Visibility of Linear Features in SAR Images, IGARSS '88, Edinburgh.

Koch K.R., Schmidt M. [1994]: Deterministische und stochastische Signale, Dümmler, Bonn.

Kwok R. [1989]: Segmentation of SAR Images, IGARSS '89, Vancouver, pp. 1228-1230.

Köster M. [1995]: Kontextsensitive Bildinterpretation mit Markoff-Zufallsfeldern, Deutsche Geodätische Kommission, C, No. 444, 76 pages.

Lakshmanan S., Derin H. [1993]: Gaussian Markov Random Fields at Multiple Resolutions, in: Chellappa R., Jain A., Markov Random Fields. Theory and Applications, Academic Press, Boston, pp. 131-157.

Leberl F. W. [1990]: Radargrammetric Image Processing, Artech House, Norwood, MA.

Lopes A., Nezry E., Touzi R., Laur H. [1993]: Structure Detection and Statistical Adaptive Speckle Filtering in SAR Images, Int. J. of Remote Sensing, Vol. 14, No. 9, pp. 1735-1758.

Oliver C. J. [1991]: Information from SAR Images, J. of Physics D, Applied Physics, Vol. 24, No. 9, pp. 1493-1514.

Quegan S., Hendry A., Skingley J. [1986]: Analysis of Synthetic Aperture Radar Images Over Land, Mathematics in Remote Sensing, Proc., Danbury, pp. 365-379.

Richards J.A. [1993]: Remote Sensing Digital Image Analysis, Springer Verlag, Berlin, 2nd edition, 340 pages.

Samadani R., Vesecky J. F. [1990]: Finding Curvilinear Features in Speckled Images, IEEE Transactions on Geoscience and Remote Sensing, Vol. 28, No. 4, pp. 669-673.

Schistad Solberg A.H., Taxt T. [1994]: Classification of Multisource Satellite Imagery Based on a Markov Random Field Model, Image and Signal Processing for Remote Sensing, Rome, SPIE Proc., Vol. 2315, pp. 322-331.

Skingley J., Rye A. J. [1987]: The Hough Transform Applied to SAR Images for Thin Line Detection, Pattern Recognition Letters, Vol. 6, No. 1, pp. 61-67.

Tough R.J.A., Blacknell D., Quegan S. [1994a]: Polarimetric Radar: Mathematical Models and their Consequences, submitted to the Proceedings of the Royal Society.

Tough R.J.A., Blacknell D., Quegan S. [1994b]: Estimators and Distributions in Single and Multi-Look Polarimetric and Interferometric Data, IGARSS '94, Pasadena, Electronical Digest.

Touzi R., Lopes A., Bousquet P. [1988]: A Statistical and Geometrical Edge Detector for SAR Images, IEEE Transactions on Geoscience and Remote Sensing, Vol. 26, No. 6, pp. 764-773.

Williams L.R., Jacobs D.W. [1995]: Stochastic Completion Fields: A Neural Model of Illusory Contour Shape and Salience, 5th ICCV, Cambridge, pp. 408-415.

Winkler G. [1995]: Image Analysis, Random Fields and Dynamic Monte Carlo Methods, Applications of Mathematics, Vol. 27, Springer-Verlag, Berlin.

Wood J. W. [1985]: Line Finding Algorithms for SAR, Royal Signals and Radar Est., St. Andrews Rd., Great Malvern, Worcestershire, England, RSRE Memorandum No. 3841.

Fig. 6.1. Synthetic line image generated by Gibbs sampling from the prior distribution. Different grey values/colors show different line states.

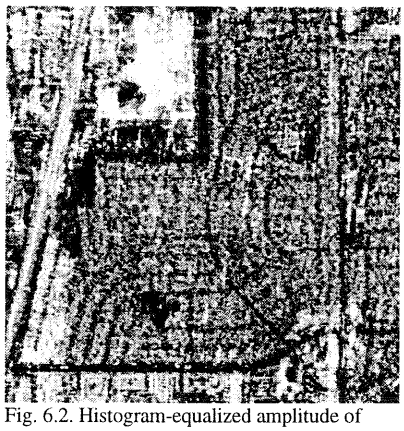

Fig. 6.2. Histogram-equalized amplitude of TOPSAR scene of 94/08/05.

Fig. 6.3. Histogram-equalized coherence of TOPSAR scene of 94/08/05.

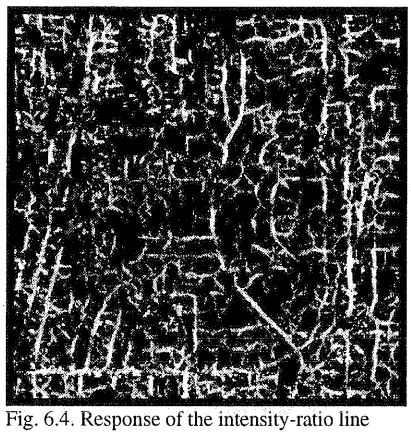

Fig. 6.4. Response of the intensity-ratio line detector.

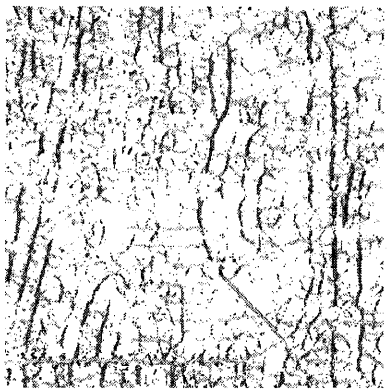

Fig. 6.5. Maximum-likelihood classification of the intensity (without utilization of prior knowledge).

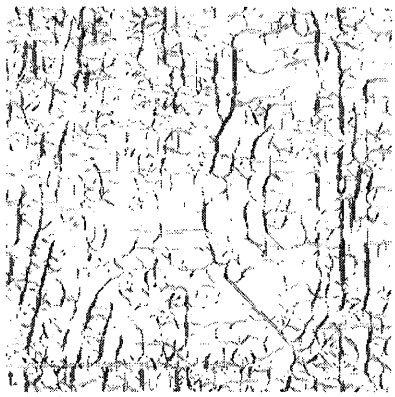

Fig. 6.6. Result of MAP estimation using simulated annealing based on intensity and generic prior knowledge.

Fig. 6.7. Result of MAP estimation using simulated annealing based on intensity, coherence and generic prior knowledge.

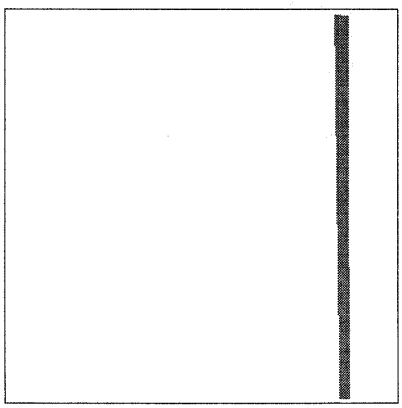

Fig. 6.8. Corridor along road center line given in a GIS.

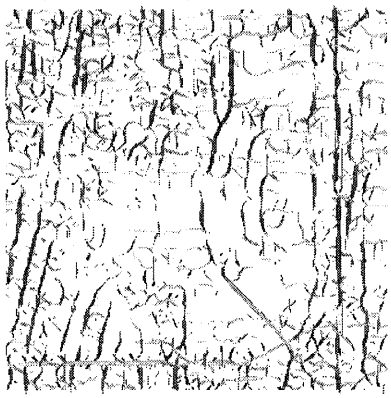

Fig. 6.9. Result of MAP estimation using simulated annealing based on intensity, coherence, GIS information and generic prior knowledge.